

## ORIGINAL ARTICLE

# Hot-electron emission-driven energy recycling in transparent plasmonic electrode for organic solar cells

Jing-De Chen<sup>1</sup> | Ling Li<sup>1</sup> | Chao-Chao Qin<sup>2</sup> | Hao Ren<sup>1</sup> | Yan-Qing Li<sup>3</sup> |  
Qing-Dong Ou<sup>4</sup>  | Jia-Jia Guo<sup>2</sup> | Shi-Jie Zou<sup>1</sup> | Feng-Ming Xie<sup>1</sup> |  
Xianjie Liu<sup>5</sup> | Jian-Xin Tang<sup>1,6</sup> 

<sup>1</sup>Jiangsu Key Laboratory for Carbon-Based Functional Materials & Devices, Institute of Functional Nano & Soft Materials (FUNSOM), Soochow University, Suzhou, Jiangsu, China

<sup>2</sup>College of Physics and Materials Science, Henan Normal University, Xinxiang, Henan, China

<sup>3</sup>School of Physics and Electronic Science, Ministry of Education Nanophotonics & Advanced Instrument Engineering Research Center, East China Normal University, Shanghai, China

<sup>4</sup>Department of Materials Science and Engineering, Monash University, Clayton, Victoria, Australia

<sup>5</sup>Laboratory of Organic Electronics, Department of Science and Technology (ITN), Linköping University, Norrköping, Sweden

<sup>6</sup>Macao Institute of Materials Science and Engineering (MIMSE), Macau University of Science and Technology, Taipa, Macau SAR, China

## Correspondence

Jian-Xin Tang, Jiangsu Key Laboratory for Carbon-Based Functional Materials & Devices, Institute of Functional Nano & Soft Materials (FUNSOM), Soochow University, Suzhou, Jiangsu 215123, China.  
Email: jxtang@suda.edu.cn

Yan-Qing Li, School of Physics and Electronic Science, Ministry of Education Nanophotonics & Advanced Instrument Engineering Research Center, East China Normal University, Shanghai 200062, China.  
Email: yqli@phy.ecnu.edu.cn

## Funding information

ARC Centre of Excellence for Future Low-Energy Electronics Technologies (FLEET); Collaborative Innovation Center of Suzhou Nano Science & Technology; Jiangsu Provincial Research Scheme of Natural Science for Higher Education Institutions, Grant/Award Number: 19KJB510056; the Natural Science Foundation of Jiangsu Province of China, Grant/Award Number: BK20190815; the 333 program, Grant/Award Number: BRA2019061; National Natural Science Foundation of China, Grant/Award Numbers: 11804084, 12074104, 62075061, 61905171, 51873138

## Abstract

Plasmonic metal electrodes with subwavelength nanostructures are promising for enhancing light harvesting in photovoltaics. However, the nonradiative damping of surface plasmon polaritons (SPPs) during coupling with sunlight results in the conversion of the excited hot-electrons to heat, which limits the absorption of light and generation of photocurrent. Herein, an energy recycling strategy driven by hot-electron emission for recycling the SPP energy trapped in the plasmonic electrodes is proposed. A transparent silver-based plasmonic metal electrode (A-PME) with a periodic hexagonal nanopore array is constructed, which is combined with a luminescent organic emitter for radiative recombination of the injected hot-electrons. Owing to the suppressed SPP energy loss via broadband hot-electron emission, the A-PME achieves an optimized optical transmission with an average transmittance of over 80% from 380 to 1200 nm. Moreover, the indium-tin-oxide-free organic solar cells yield an enhanced light harvesting with a power conversion efficiency of 16.1%.

## KEYWORDS

energy recycling, hot-electron emission, organic solar cells, plasmonic electrode, surface plasmon polariton

Jing-De Chen and Ling Li contributed equally to this work.

This is an open access article under the terms of the Creative Commons Attribution License, which permits use, distribution and reproduction in any medium, provided the original work is properly cited.

© 2022 The Authors. *InfoMat* published by UESTC and John Wiley & Sons Australia, Ltd.

## 1 | INTRODUCTION

Owing to their high conductivity, excellent malleability, and good processing compatibility with various rigid and flexible substrates, metal electrodes are widely used as electrodes in optoelectronic devices, such as organic solar cells (OSCs), perovskite solar cells, light-emitting diodes, and photodetectors.<sup>1–7</sup> However, the highly reflective nature of metal electrodes (e.g., silver and gold) leads to the interfacial reflection of incident light and limited optical absorption, specifically for their application as a front transparent electrode in OSCs.<sup>6–8</sup> Therefore, to solve this problem and improve the light harvesting efficiency in OSCs, structured metal electrodes such as wrinkle, grating, nanopore, and moth-eye have been introduced to manipulate the incident light to reduce the reflection and enhancing the effective optical path in the absorbers.<sup>9–13</sup> In particular, plasmonic metal electrodes (PMEs) with periodic subwavelength nanostructures have gained significant importance in solar cells owing to their superior ability of guiding and localizing the incident light to surface plasmon polaritons (SPPs).<sup>13,14</sup>

PMEs can act as scattering centers favorable for trapping the incident light inside photovoltaic devices through radiative damping of SPPs in leaky modes.<sup>15,16</sup> However, SPPs in bound modes cannot contribute to the optical absorption of the absorber because their exponential decay propagating along the metal surface causes nonradiative damping.<sup>17,18</sup> The trapped light in PME is lost owing to the dephasing of SPPs and their conversion into heat.<sup>7,8,19–21</sup> Therefore, it is necessary to develop novel strategies for recycling the SPP energy and restraining the nonradiative damping in PME for the optimization of OSCs.

After the scattering of the oscillating electrons by the free electrons in plasmonic metal nanostructures, the SPP energy is transferred to the free electrons, generating an excited hot-electron.<sup>22–24</sup> Therefore, the effective collection of hot-electrons is essential for the energy recycling in PME and the suppression of energy loss. In this study, an injection mechanism of hot-electrons (left of Figure 1A) was proposed, in which the photogenerated hot-electrons with an energy higher than the Schottky barrier ( $\phi_b$ ) can be transferred from the metal Fermi level ( $E_F$ ) to the lowest unoccupied molecular orbital (LUMO) of an adjacent nonluminescent semiconductor (NL-SC).<sup>25–28</sup> However, the hot-electrons generated at the front PME were rarely collected by the rear electrode because of the long drift length through the hole-transport layer (HTL), the active layer, and the electron-transport layer (ETL) (left of Figure 1B). The injected hot-electrons were generally trapped around the PME via nonradiative recombination, and the SPP energy was lost via heat.<sup>19,29</sup>

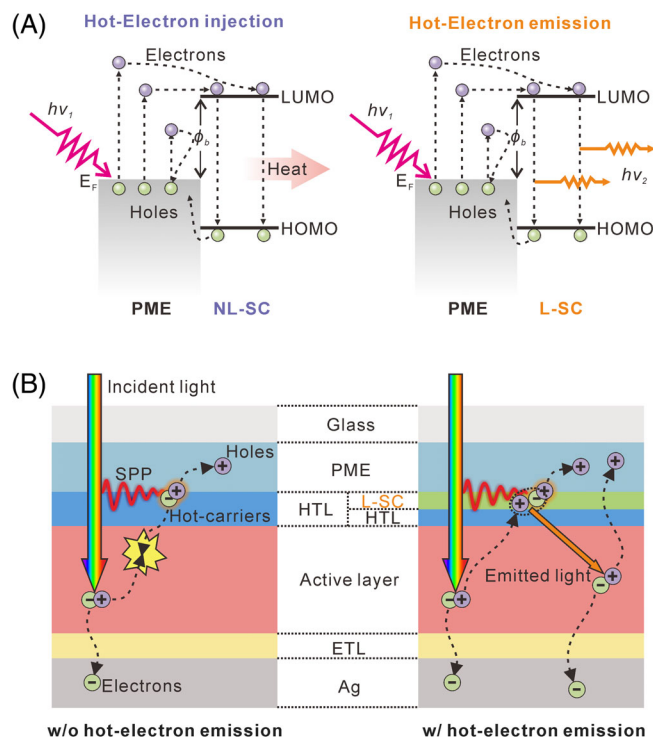


**FIGURE 1** Mechanisms of hot-electron emission-driven energy harvesting. (A) Diagrams of carrier dynamics of hot-electron injection and hot-electron emission in operating OSCs. (B) Schematic energy-harvesting processes in OSCs without and with hot-electron emission

To utilize the injected hot-electrons fully, a hot-electron emission approach was first proposed to recycle the SPP energy trapped in the PME for the realization of efficient OSCs. The carrier dynamics of a hot-electron emission in operating OSCs are schematically shown on the right of Figure 1A. A luminescent semiconductor (L-SC) is in close contact with PME. When the device is illuminated, SPPs are excited and relaxed by generating hot-electrons. The hot-electrons with energies larger than the Schottky barrier could be injected into the L-SC and occupy the LUMO. Thereafter, radiative recombination occurs owing to the recombination of the injected hot-electrons and photogenerated holes that are located at the highest occupied molecular orbital (HOMO). When the wavelength of the emitted light is covered by the absorption spectrum of the active layer, the hot-electron-induced emission from the L-SC can be harvested for the generation of photocurrent in OSCs. As a result, the SPP energy can be effectively recycled, as illustrated on the right of Figure 1B. To experimentally realize this method in OSCs, a silver-based PME (A-PME) with a hexagonal nanopore array was fabricated according to a previous report,<sup>19</sup> and a yellow-emission organic molecule, 2,8-ditertbutyl-5,11-bis(4-tert-butylphenyl)-6,12-diphenyltetracene (TBRb), was used as the adjacent L-SC for the injection and emission of hot-electrons. The SPP energy loss in the A-PME can be recycled because

of the TBRb-induced hot-electron emission, which is demonstrated by the photoluminescence (PL), transient absorption (TA), and simulation results. Therefore, the A-PME with an optimized nanopore array achieves broadband optical transmission with an average transmittance of 80.3% from 380 to 1200 nm. Moreover, the hot-electron emission in the A-PME/TBRb system can be absorbed effectively by the active layer of OSCs and converted to photocurrent, leading to an increase in the short current density ( $J_{SC}$ ) and an optimized power conversion efficiency (PCE) of 16.1% for the PM6:N3:PC<sub>71</sub>BM-based OSCs.

## 2 | RESULTS AND DISCUSSION

Figure 2A shows a schematic fabrication of the A-PME with a hexagonal nanopore array. A close-packed

polystyrene (PS) sphere array was assembled on a glass substrate and etched via reactive ion etching (RIE). The etched PS sphere array acted as a shadow mask during the thermal evaporation of Ag film. According to previous reports,<sup>6,30,31</sup> a seeding layer with 5 nm-thick Al<sub>2</sub>O<sub>3</sub> and 0.5 nm-thick Al was deposited on the glass substrate to facilitate the uniform formation of the Ag film. Moreover, the adhesion of the nanostructured Ag film on the glass substrate was enhanced, enabling the structural integrity of the Ag film even after the solution processing of other functional layers. Finally, the A-PME was obtained after removing the PS spheres. The parameters of the hexagonal nanopore array in A-PMEs can be optimized by modifying the layer thickness, surface coverage, and structural periodicity. In this study, the surface coverage of the PS sphere array on the substrate was controlled to be approximately 50% by rationally tuning the

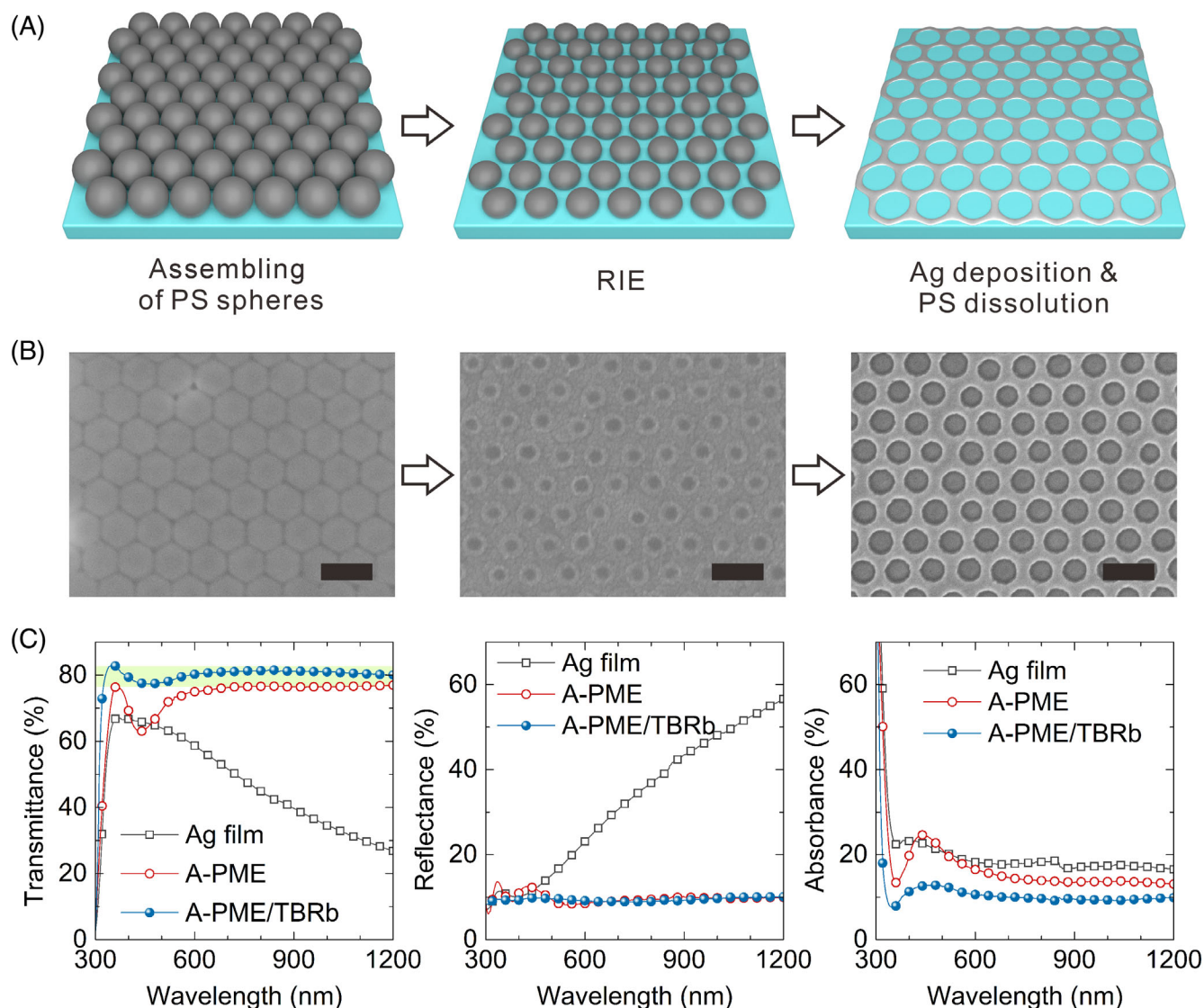


**FIGURE 2** Fabrication and optical properties of the A-PME. (A) Schematic fabrication of the A-PME. (B) SEM images of the corresponding fabrication of the A-PME using PS spheres with a diameter of 200 nm. Scale bars are 300 nm. (C) Transmission, reflection, and absorption spectra of Ag film, A-PME, and A-PME/TBRb. The green line denotes the transmittance region from 77% to 82%

etching duration, and the thickness of the deposited Ag film was maintained at 12 nm to achieve a relatively low square resistance ( $R_{sq}$ ). By balancing the film morphology, electrical conductivity, and optical transparency, a structural period of 200 nm was selected for the A-PME as a transparent electrode in OSCs.

Figure 2B shows the scanning electron microscopy (SEM) images of the substrates during each fabrication step for the A-PME using PS spheres with a diameter of 200 nm. As shown in Figure S1, the periods of the hexagonal nanopore arrays can be controlled using the PS spheres with various diameters. The A-PME in this study has a 200 nm period nanopore array. Notably, A-PMEs exhibit uniform film morphology, although cracks and bumps can be observed with a decrease in the array period, which is ascribed to the shadow effect of the etched PS spheres. Additionally, atomic force microscopy (AFM) was employed to characterize the morphology of the A-PME (Figure S2A), revealing a surface arithmetic mean deviation roughness of 4.03 nm. In addition, the  $R_{sq}$  value of the corresponding A-PME is  $\sim 31.2 \Omega \text{ sq}^{-1}$ , which satisfies the requirement of being an electrode.

The optical properties of the A-PMEs were characterized, and a nonpatterned Ag film (thickness of 12 nm) was used as the reference. As shown in Figure 2C, the transmittance of a nonpatterned Ag film exhibits a peak value of 67.2% at 368 nm and it decreases to 26.8% when the wavelength increases to 1200 nm. In contrast, the optical transmittance of A-PME with a period of 200 nm significantly increases, specifically in the near-infrared region, which originates from the significantly suppressed reflection (Figure 2C). Consequently, the average transmittance ( $T_{ave}$ , from 380 to 1200 nm) increases from 46.9% for the nonpatterned Ag film to 72.9% for the A-PME. Notably, the A-PME exhibits a characteristic transmission valley in the visible region, which is attributed to the enhanced SPP-induced absorption (Figure 2C).

The optical properties of the various electrodes were theoretically simulated to clarify the influence of the structural periodicity on the SPP modulation. The finite-difference time-domain (FDTD) method was employed with a structural setup and the polarization direction of the applied light source, as shown in Figure S3. The simulated transmission spectra of A-PMEs (Figure S4A) show a distinct feature in that the transmission valley is blue-shifted as the period of the hexagonal nanopore array decreases. The simulated absorption spectra exhibit similar phenomena (Figure S4C), and the characteristic absorption peak is ascribed to the SPP mode, which is related to the geometry of the periodic structure. Moreover, the simulation results indicate that the hexagonal periodic nanopore arrays can couple the incident light to SPPs and suppress the reflection in the full spectrum. In

a hexagonally periodic structure, the SPP resonance is excited when equation  $\mathbf{k}_{SPP} = \mathbf{k}_0 \pm m\mathbf{b}_1 \pm n\mathbf{b}_2$  is satisfied, where  $\mathbf{k}_{SPP}$  and  $\mathbf{k}_0$  are the wave vectors of the SPPs and incident light, respectively;  $\mathbf{b}_1$  and  $\mathbf{b}_2$  are the reciprocal lattice vectors of the periodic nanopore array;  $m$  and  $n$  are integers that determine the propagation direction of the SPPs (as indicated in Figure S5). The wave vectors are defined according to the formulas  $|\mathbf{b}_1| = |\mathbf{b}_2| = \frac{2\pi}{D}$ ,  $|\mathbf{k}_{SPP}| = \frac{\omega}{c} \left( \frac{\epsilon_0 \epsilon_m}{\epsilon_0 + \epsilon_m} \right)^{1/2}$ , and  $|\mathbf{k}_0| = \frac{\omega}{c} \epsilon_0^{1/2}$ , where  $D$  is the period of a nanopore array,  $\omega$  is the angular frequency,  $c$  is the velocity of light,  $\epsilon_0$  is the permittivity of the medium, and  $\epsilon_m$  is the permittivity of the metal.<sup>32</sup> Accordingly, the resonance frequency of the SPPs increases with the decrease in  $D$ , and the absorption peak around 400–500 nm originates from the overlapping of the SPP resonance modes of  $(m, n) = (1, 0), (0, 1), (1, 1), \text{ and } (1, 2)$ . This indicates that incident light with an appropriate wavelength and electric field component that is parallel to the  $(m, n)$  direction can excite SPPs on the surface of A-PMEs.<sup>33</sup> Moreover, the decrease in the array period merges multiple discrete SPP peaks into a single broad peak (Figure S4), revealing that the transmission valley stems from the SPP damping of the A-PMEs. To verify the generation of SPPs in A-PMEs further, the distribution profiles of the  $z$  component (perpendicular to the substrate surface) of the electric field ( $E_z$ ) for various electrodes were simulated under the illumination of polarized light with different wavelengths. There is no  $E_z$  signal for the nonpatterned Ag film (Figure S6A), whereas remarkable  $E_z$  distribution profiles can be observed at the geometric focus of the Ag strips for various A-PMEs at the corresponding absorption peaks (Figure S6B–D). These local electric field enhancements represent the hallmark of the SPP resonance. The generation of the SPPs was also observed in A-PMEs under illumination with 700 and 900 nm polarized light (Figure S7), indicating the full-spectrum excitation phenomenon of the SPPs in A-PMEs. Aperiodic A-PME was fabricated and characterized to determine the role of localized surface plasmon resonance in optical engineering (Figure S8). No significant absorption peak was found in the optical spectra, suggesting that the plasmonic resonance in A-PME is dominated by SPPs.

To develop the hot-electron emission system, a 2 nm-thick TBRb film was deposited on the A-PME with a period of 200 nm. The surface arithmetic mean deviation roughness of A-PME/TBRb is approximate 4.29 nm, indicating the negligible influence of TBRb on the morphology of A-PME (Figure S2B). Moreover, the conformal surface morphologies of A-PME and A-PME/TBRb exhibit good physical contact between A-PME and TBRb. The optical properties of A-PME/TBRb were characterized and they are plotted in Figure 2C. Compared to the bare A-PME, the transmission of A-PME/TBRb significantly improved,



specifically in the wavelength region from 400 to 600 nm (at the main resonance peak of SPPs). The reflection and absorption of A-PME/TBRb were simultaneously suppressed by an additional TBRb layer. Moreover, the A-PME/TBRb system shows a wavelength-independent transmission feature, and its transmittance ranges approximately from 77% to 82% in the wavelength region ranging from 330 to 1200 nm. A peak transmittance approaching 82.9% and a  $T_{\text{ave}}$  of 80.3% (380–1200 nm) were obtained, which are 71% higher than that of the nonpatterned Ag film. In addition, the influence of TBRb on the optical properties of A-PME was simulated (Figure S4). It was established that the TBRb layer hardly affected the transmission, although it caused a red-shift of the main SPP peak. Therefore, the increase in transmission may be ascribed to the SPP energy recycling, which reduces the absorption of A-PME rather than the optical engineering effect of TBRb.

The origin of the improved optical transmission was investigated by characterizing the PL spectra of A-PME/TBRb, TBRb, and Ag film/TBRb under different excitation light sources. TBRb has an absorption edge at 560 nm, corresponding to an optical band gap of 2.2 eV, and an emission peak at 570 nm (Figure S9). Under illumination with 400 nm light, TBRb showed a PL peak at 565 nm on different substrates (Figure 3A). Notably, the PL intensity of the A-PME/TBRb system is 3.5 times higher than that of the bare TBRb film, whereas the Ag film/TBRb exhibits a clearly reduced PL intensity. Similar phenomena were observed in the PL spectra under an excitation of 500 nm light (Figure S10A). When the PL measurements were performed under excitation light with a wavelength beyond the absorption edge of TBRb (700 and 800 nm), no emission was detected for the bare TBRb and Ag film/TBRb (Figure 3B and Figure S10B). In contrast, the PL signals originating from TBRb were clearly observed for the A-PME/TBRb. To investigate the origin of the enhanced PL intensity for the A-PME/TBRb system, a 2 nm-thick  $\text{Al}_2\text{O}_3$  was inserted between A-PME and TBRb, which was used to block the direct hot-electron injection from TBRb to A-PME. As compared to the A-PME/TBRb, the PL intensity for A-PME/ $\text{Al}_2\text{O}_3$ /TBRb is significantly decreased and similar to that of TBRb (Figure S11). As hot-electron injection is highly limited by the intimate contact between the plasmonic structure and the semiconductor,<sup>34,35</sup> the  $\text{Al}_2\text{O}_3$ -induced PL decrease indicates that hot-electron emission dominates the luminescence of the A-PME/TBRb, whereas the plasmon energy transfer has small contribution to the recycling of SPP energy. In addition, the plasmon energy transfer is present only when the band gap of the semiconductor overlaps the plasmonic band. For the A-PME/TBRb illuminated under 800 nm light, the plasmonic band is smaller than the band gap of TBRb. Therefore, the

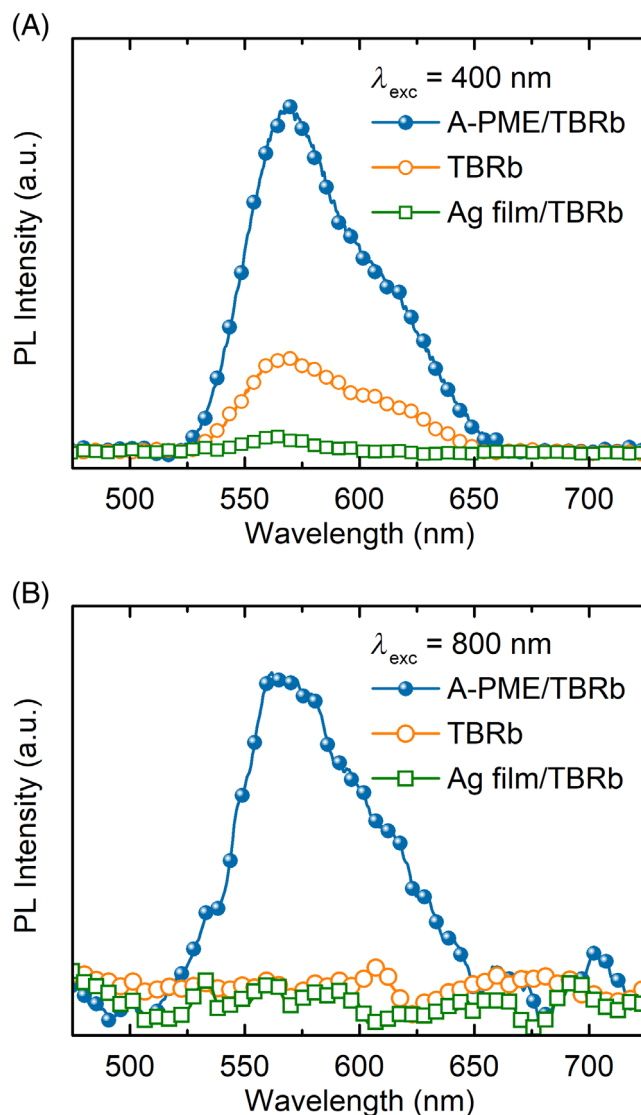


**FIGURE 3** Hot-electron emission in the A-PME/TBRb system. PL spectra of the A-PME/TBRb, TBRb, and Ag film/TBRb under the excitation at wavelengths of (A) 400 nm and (B) 800 nm

up-conversion phenomenon could originate from hot-electron emission rather than the plasmon energy transfer. Consequently, the TBRb emission for the A-PME/TBRb system under long-wavelength illumination could mainly arise from the existence of hot-electron emission owing to the extra injection of hot-electrons from A-PME to TBRb. Additionally, the transmission enhancement for the A-PME/TBRb is mainly attributed to the hot-electrons from SPPs. One photon absorption (1PA) in the short-wavelength region and two photon absorption (2PA) in the long-wavelength region could improve the luminescence.<sup>36–40</sup> However, the nonpatterned Ag film causes near-field light trapping of the emission from TBRb by coupling the emission into SPPs, decreasing the PL intensity in the Ag film/TBRb. In addition, the low transmittance of the flat Ag film reduces the intensity of incident light that irradiates on

TBRb and it further suppresses the PL intensity of A-PME/TBRb.

To understand the dynamics of the hot-electron emissions in A-PME/TBRb further, TA measurements were performed. A laser pump with a wavelength of 620 nm, which was beyond the absorption region of TBRb but could excite the SPPs in the A-PME, was employed. Figure 4A–C show the ultrafast TA maps in the form of differential absorbance of TBRb, A-PME, and A-PME/TBRb. The TA delay ( $\Delta A$ ) in unit of milli-optical density (mOD) can be calculated according to the equation  $\Delta A = -\log(T/T_0)$ , where  $T$  and  $T_0$  are the measured transmittance of the sample with and without the pump pulse, respectively. No  $\Delta A$  response was detected from bare TBRb film, indicating carrier cannot be excited in TBRb under irradiation of 620 nm light (Figure 4A). On the contrary, a significant  $\Delta A$  response (blue region in Figure 4B) is observed in the TA profile of A-PME, indicating ground state bleaching. The high  $\Delta A$  from 350 to 450 nm is ascribed to the generation of SPPs and excitation of hot-electrons in A-PME because TBRb cannot emit light within this spectral region. In addition, A-PME/TBRb exhibited a stronger TA (Figure 4C). The enhanced TA response in A-PME/TBRb is attributed to the reduction in the ground state absorption, which represents fewer electrons in the ground state. In the pumped samples, the electrons jump from the ground to excited states, and the relaxation of electrons from the excited to the ground states occurs simultaneously. TBRb extracts hot-electrons from A-PME on a femtosecond time scale, and then reduces the population of electrons in the excited states. The possibility of electron relaxation to the ground state is decreased, resulting in fewer electrons in the ground state. Therefore, an improved TA response is observed for the A-PME/TBRb.

To understand the carrier dynamics, the TA decays of A-PME and A-PME/TBRb were extracted from the TA profiles and then they were compared (Figure S12). The TA response was hardly detected when the A-PME was probed at 550 nm, whereas it was clear in A-PME/TBRb. This result indicates that the response of A-PME/TBRb at 550 nm is mainly ascribed to the emission of TBRb because bare TBRb has no TA response. Thus, the hot-electrons injected from the A-PME fill the unoccupied molecular orbitals and then transfer to the LUMO of TBRb. Luminescence at approximately 550 nm occurs during the rapid radiative relaxation of the electrons from LUMO to HOMO, resulting in an ultrashort lifetime for hot-electrons detected at 550 nm. By comparing the normalized decay profiles, it was established that the  $\Delta A$  of A-PME and A-PME/TBRb detected at 400 nm have a similar decay tendency, whereas that of A-PME/TBRb detected at 550 nm exhibits a steeper drop. The Coulomb potential in Ag effectively suppressed

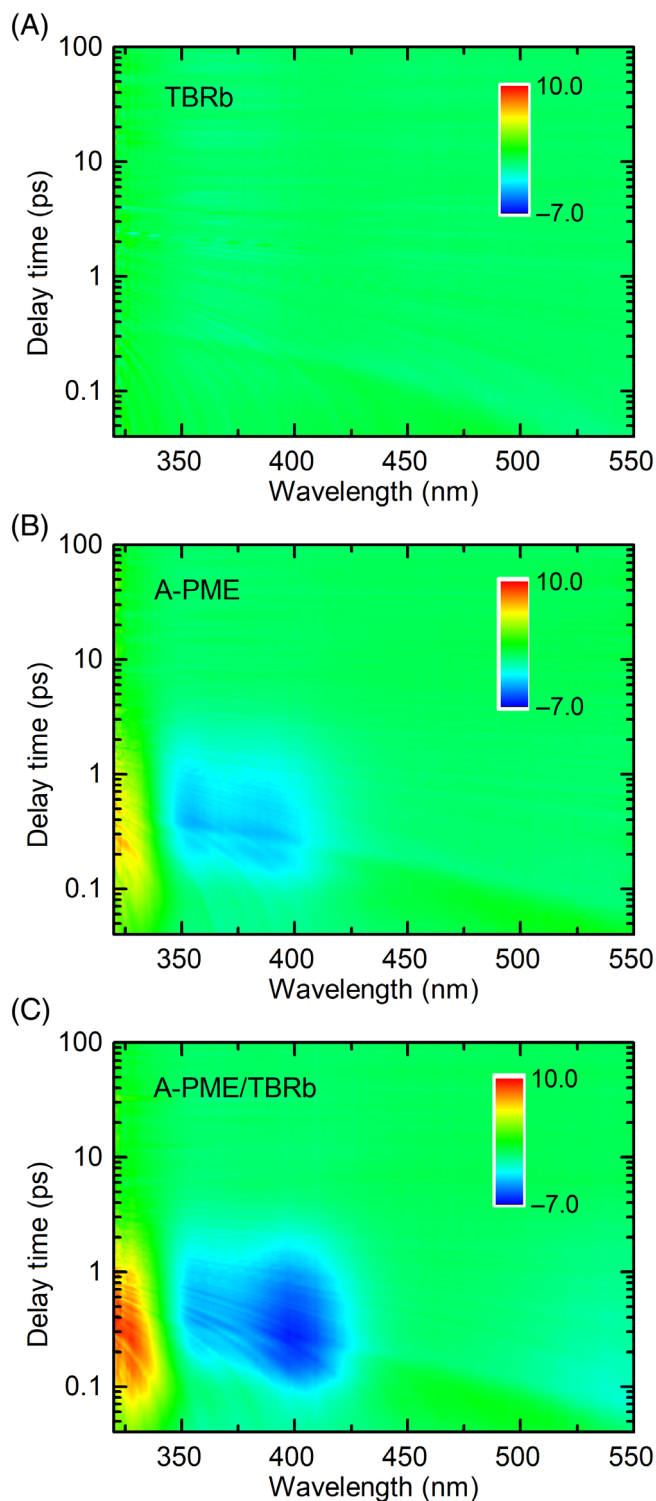


**FIGURE 4** Comparison of TA properties of TBRb and A-PME/TBRb. Two-dimensional pseudo-color maps of differential absorbance of (A) TBRb, (B) A-PME, and (C) A-PME/TBRb. The scale bar corresponds to the intensity of  $\Delta A$

the electron-hole recombination of hot-electrons in A-PME.<sup>41</sup> Consequently, the electron-phonon scattering dominates the relaxation of hot-electrons in A-PME and leads to relatively longer lifetime of the signal at 400 nm.

Owing to the high optical transmittance and the presence of hot-electron emission, the A-PME/TBRb system is a promising transparent electrode in OSCs. To verify its applicability, indium-tin-oxide-free OSCs were fabricated using the architecture of glass/transparent electrode/molybdenum oxide ( $\text{MoO}_3$ )/PM6:N3:PC<sub>71</sub>BM/PDINO/Ag. Here, a transition metal oxide interface layer of  $\text{MoO}_3$  was deposited on top of the TBRb L-SC to act as the HTL, which can match the HOMO levels between TBRb and the active layer for efficient hole extraction without the additional energy loss at the interface (Figure S13). The photovoltaic performance of OSCs was measured under the illumination of air-mass 1.5 global (AM 1.5G) solar illumination with a power density of  $100 \text{ mW cm}^{-2}$ . Figure 5A shows the current density–voltage (J–V) curves of OSCs fabricated on various electrodes, and the corresponding external quantum efficiency (EQE) spectra are shown in Figure 5B. The detailed performance parameters deduced from the J–V curves are listed in Table 1. Evidently, the OSCs with various electrodes exhibit an almost identical fill factor (FF) and open-circuit voltage ( $V_{\text{OC}}$ ), indicating the similar electrical properties of the transparent electrodes. The nonpatterned Ag film-based device showed poor device performance, specifically a  $J_{\text{SC}}$  of  $17.8 \text{ mA cm}^{-2}$ , which is attributed to the low transmission of the nonpatterned Ag film in the long-wavelength region (Figure 2C). For comparison, the device performance was significantly improved using the A-PME, and it exhibited an enhanced  $J_{\text{SC}}$  of  $22.9 \text{ mA cm}^{-2}$ . The addition of TBRb L-SC increases  $J_{\text{SC}}$  to  $24.3 \text{ mA cm}^{-2}$ . Owing to the excitation and energy recycling of SPPs, the optimized OSCs significantly suppressed the energy loss, and its PCE increased by 36.4% and 5.9% as compared to those of Ag film- and A-PME-based devices, respectively. As a result, the PCE of the A-PME/TBRb-based OSC was optimized to 16.1%, which is comparable to those for PM6:N3:PC<sub>71</sub>BM-based devices on indium-tin-oxide glass.<sup>42,43</sup> The integrated  $J_{\text{SC}}$  from the EQE spectra of Ag film, A-PME, and A-PME/TBRb-based OSCs are 16.8, 22.7, and  $23.7 \text{ mA cm}^{-2}$ , respectively, which are all in acceptable mismatch to the measured results. Moreover, the EQE spectrum of the A-PME/TBRb-based device reveals a broadband enhancement than that of the A-PME-based device over the region ranging from 350 to 820 nm. In particular, a significant enhancement around 400–500 nm was observed, which is consistent with the changes in the optical transmission, as shown in Figure 2C. To investigate the influence of optical engineering on device performance, the absorption spectra and electric field distribution maps of A-PME- and A-PME/TBRb-based OSCs were simulated. The results shown in Figure S14 indicate the negligible influence of TBRb on the absorption and electric field

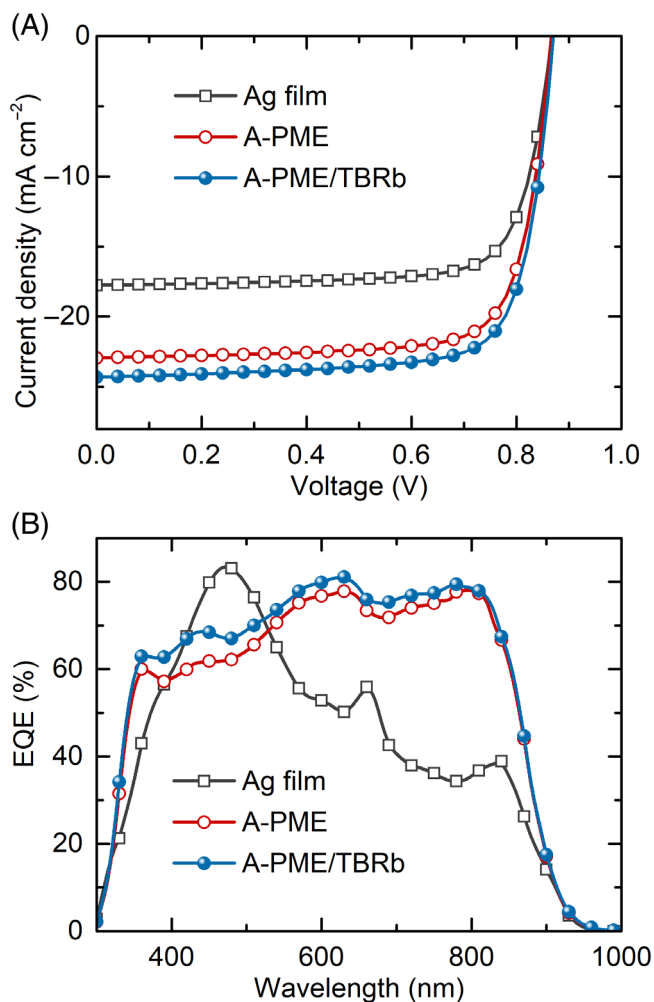


**FIGURE 5** Device performances of OSCs based on various electrodes. (A) J–V curves. (B) EQE spectra for devices with Ag film, A-PME, and A-PME/TBRb

distribution of the device. According to the proven hot-electron emission in A-PME/TBRb, the improved light harvesting in the A-PME/TBRb-based OSCs is attributed to the energy recycling by suppressing the nonradiative damping loss of SPPs in the A-PME, as illustrated in Figure 1B.

The Fermi-Dirac-like distribution of hot-electrons determines that only part of the excited hot-electrons with enough energy to overcome  $\phi_b$  can be injected from the PME into the adjacent L-SC. Because the work functions of Ag and the LUMO energy of TBRb are  $\sim 4.2$  and  $\sim 3.2 \text{ eV}$ ,<sup>44</sup> respectively, the incident with an energy larger than  $1.0 \text{ eV}$  ( $\phi_b = 1.0 \text{ eV}$ ) could promote the injection of hot-electrons from A-PME into TBRb for the hot-electron emission. To verify the hole–electron emission-driven energy recycling in the A-PME/TBRb-based OSCs further, an active layer with a narrower EQE response was applied. OSCs with an active layer of poly (3-hexylthiophene):[6,6]-phenyl C61 butyric acid methyl

Electrode	$V_{OC}$ (V)	$J_{SC}$ ( $\text{mA cm}^{-2}$ )	FF (%)	PCE (%)	PCE <sub>ave</sub> (%)
Ag film	0.867	17.8	76.6	11.8	11.2
A-PME	0.867	22.9	76.5	15.2	14.4
A-PME/TBRb	0.869	24.3	76.1	16.1	15.4

Note: Average PCEs (PCE<sub>ave</sub>) are obtained based on six devices.

**TABLE 1** Photovoltaic characteristics of various OSCs under the illumination of AM 1.5 G with an intensity of  $100 \text{ mW cm}^{-2}$

ester (P3HT:PCBM) were fabricated, and a similar photovoltaic enhancement was obtained for the A-PME/TBRb-based device, as shown in Figure S15. Evidently, the enhanced  $J_{SC}$  in the A-PME/TBRb-based device arises from the broadband enhancement in EQE between 350 and 700 nm. In particular, there is a significant EQE enhancement in the region of 650 and 700 nm for the A-PME/TBRb-based OSC. Because the wavelength around 700 nm is beyond the absorption of the P3HT:PCBM active layer, the enhanced EQE in this region indicates the hot-electron emission for recycling the SPP energy loss in A-PME, improving the PCE of A-PME/TBRb-based OSCs.

Additionally, the SPP energy recycling efficiency was estimated. Assuming that all the photons absorbed by A-PME can generate SPPs, the photon energy is considered as the energy of the SPPs. The absorption of the A-PME can be regarded as the power distribution of the SPPs. With the conjecture that all the growth of photo-generated current originates from the SPP energy recycling, the energy recycling efficiency can be calculated by dividing the absorption with increase of EQE. As shown in Figure S16, the energy recycling efficiency reached a maximum value of 30% at a wavelength of 400 nm, and it gradually decreased as the wavelength increased. This is consistent with the model of hot-electron emission because the hot-electron injection efficiency reduces as the photon energy decreases.

### 3 | CONCLUSION

In summary, a hot-electron emission-driven energy recycling strategy has been demonstrated to release the trapped SPP energy in transparent plasmonic electrodes for efficient light harvesting in OSCs. The conventional nonradiative damping of SPPs can be effectively restrained in the nanostructured A-PME/TBRb system by converting the SPPs via broadband hot-electron emission from the TBRb emitter. Thus, the light absorption and photocurrent generation are significantly enhanced in OSCs. The optimized OSCs achieve a PCE of 16.1% owing to the reduced SPP energy loss. We anticipate that the method proposed in this study improves the optical properties of plasmonic electrodes and recycles the SPP energy for efficient light harvesting in optoelectronic devices.

## 4 | EXPERIMENTAL SECTION

### 4.1 | Electrode fabrication

The PS nanosphere solution (Huge Biotechnology GmbH, 5 wt%) was diluted with ethanol at a ratio of 1:1.5 prior to use. An ultraviolet (UV) ozone-treated Si wafer was placed beneath the surface of deionized (DI) water. The prepared PS ethanol solution was dripped to the center of the Si wafer. After 10 min of assembly, monolayered PS nanospheres were formed at the air/water interface. Thereafter, the dodecyl sodium sulfate solution (2%, 3 ml) was dripped slowly into the DI water to change its surface tension and promote close-packing of the PS spheres. After the wafer was gently removed, a 5 nm  $\text{Al}_2\text{O}_3$ -coated glass prepared via an atomic layer deposition technique was placed below the floating PS spheres and slowly pulled up at an oblique angle of approximately  $45^\circ$ . Close-packed PS arrays were obtained after evaporating the residual water on the glass. The PS sphere arrays were etched in a plasma reactor (Plasmalab 80 plus machine, OXFORD company with 40 sccm oxygen at 45 W under a pressure of  $5 \times 10^{-5}$  Torr) for various durations to fabricate PS sphere arrays with a surface coverage of approximately 50%. Afterward, 0.5 nm Al and 12 nm Ag were thermally deposited onto the samples under a pressure below  $4 \times 10^{-6}$  Torr. Finally, A-PMEs were obtained after removing the PS spheres by ultrasonication the samples in methylbenzene.

### 4.2 | Device fabrication

For indium-tin-oxide-free OSCs, 2 nm-thick 2,8-ditertbutyl-5,11-bis(4-tert-butylphenyl)-6,12-diphenyltetracene (TBRb) and 8 nm-thick  $\text{MoO}_3$  were thermally deposited onto the samples under a pressure below  $2 \times 10^{-6}$  Torr. The precursor solution of the active layer was prepared by dissolving poly[(2,6-(4,8-bis(4-fluoro-5-(2-ethylhexyl)thiophen-2-yl)benzo[1,2-b:4,5-b']dithiophene))-alt-(5,5-(1',3'-di-2-thienyl-5',7'-bis(2-ethylhexyl)benzo[1',2'-c:4',5'-c']-dithiophene-4,8-dione))] (PM6), N3 (a derivative of small molecule Y6 with 3rd-position branched alkyl chains), and [6,6]-phenyl C71-butyric acid methyl ester ( $\text{PC}_{71}\text{BM}$ ) at a ratio of 1:0.96:0.24 in chlorobenzene and naphthalene chloride at  $65^\circ\text{C}$  with continuous stirring for approximately



2 h. The precursor was spin-coated on MoO<sub>3</sub> at 1500 rpm for 45 s in a nitrogen-filled glovebox. The samples were then placed in a vacuum chamber for approximately 5 min and annealed at 90°C for 5 min, and a solid-state active layer was formed. Thereafter, the 2,9-Bis[3-(dimethyloxidoamino)propyl]anthra[2,1,9-def:6,5,10-d'e'f']diisoquinoline-1,3,8,10(2H,9H)-tetrone (PDINO) solution (1 mg ml<sup>-1</sup> in methanol) was spin-coated at 3000 rpm for 45 s to act as an ETL. Finally, the complete devices were fabricated by thermally evaporating 100 nm-thick Ag onto the samples under a chamber pressure of  $2 \times 10^{-6}$  Torr with a deposition rates of 0.4 nm s<sup>-1</sup>. Shadow masks with an effective area of 0.0725 cm<sup>2</sup> were used to determine the pattern of the top Ag electrode.

### 4.3 | Characterization

Optical spectra were measured via a UV-vis-NIR spectrometer (Perkin Elmer Lambda 950) with an integrating sphere. The surface morphologies of the samples were characterized via SEM (Carl Zeiss, Merlin) and AFM (Veeco, MultiMode V). J-V curves were recorded using a programmable Keithley 2612 source measurement unit under the illumination of AM 1.5G with a power of 100 mW cm<sup>-2</sup> (Newport 961 160 solar simulator). The illumination intensity of the solar simulator was calibrated using a standard Si photodiode with a known spectral response. The devices were characterized in ambient air with a relative humidity of 30% and at room temperature. A shadow mask with an open area of 0.0725 cm<sup>2</sup> was used to determine the actual illumination area of the devices during the measurements. TA measurements were performed on a Helios pump-probe system (Ultrafast Systems LLC) combined with an amplified femtosecond laser system (Coherent). The detailed set parameters can be found in a previous report.<sup>45</sup> The EQE spectra were obtained with QE-R (Enlitech). A spectrofluorometer (Horiba Jobin Yvon FL3) was used to record the PL spectra. Lumerical FDTD solution was used to perform theoretical simulations for optical field distributions.

### ACKNOWLEDGMENTS

Jing-De Chen, Ling Li, and Chao-Chao Qin contributed equally to this work. The authors acknowledge the financial support from the National Natural Science Foundation of China (Nos. 51873138, 61905171, 62075061, 12074104, 11804084), the 333 program (No. BRA2019061), the Natural Science Foundation of Jiangsu Province of China (BK20190815), Jiangsu Provincial Research Scheme of Natural Science for Higher Education Institutions (19KJB510056), and Collaborative Innovation Center of Suzhou Nano Science & Technology. Qing-Dong Ou

acknowledges support from ARC Centre of Excellence in Future Low-Energy Electronics Technologies (FLEET).

### CONFLICT OF INTEREST

The authors declare no conflict of interest.

### ORCID

Qing-Dong Ou  <https://orcid.org/0000-0003-2161-2543>

Jian-Xin Tang  <https://orcid.org/0000-0002-6813-0448>

### REFERENCES

1. Rahmany S, Etgar L. Semitransparent perovskite solar cells. *ACS Energy Lett.* 2020;5(5):1519-1531.
2. Zuo L, Shi X, Fu W, Jen AK. Highly efficient semitransparent solar cells with selective absorption and tandem architecture. *Adv Mater.* 2019;31:1901683.
3. Li Y, Ji C, Qu Y, et al. Enhanced light utilization in semitransparent organic photovoltaics using an optical outcoupling architecture. *Adv Mater.* 2019;31:1903173.
4. Wu W, Wang X, Han X, et al. Flexible photodetector arrays based on patterned CH<sub>3</sub>NH<sub>3</sub>PbI<sub>3-x</sub>Cl<sub>x</sub> perovskite film for real-time photosensing and imaging. *Adv Mater.* 2019;31:1805913.
5. Li YW, Xu GY, Cui CH, Li YF. Flexible and semitransparent organic solar cells. *Adv Energy Mater.* 2018;8:1701791.
6. Yun J. Ultrathin metal films for transparent electrodes of flexible optoelectronic devices. *Adv Funct Mater.* 2017;27:1606641.
7. Bi YG, Liu YF, Zhang XL, et al. Ultrathin metal films as the transparent electrode in ITO-free organic optoelectronic devices. *Adv Opt Mater.* 2019;7:1800778.
8. Zhang C, Kinsey N, Chen L, et al. High-performance doped silver films: overcoming fundamental material limits for nanophotonic applications. *Adv Mater.* 2017;29:1605177.
9. You JB, Li XH, Xie FX, et al. Surface plasmon and scattering-enhanced low-bandgap polymer solar cell by a metal grating back electrode. *Adv Energy Mater.* 2012;2(10):1203-1207.
10. Chen JD, Li YQ, Zhu J, et al. Polymer solar cells with 90% external quantum efficiency featuring an ideal light- and charge-manipulation layer. *Adv Mater.* 2018;30:e1706083.
11. Cao WR, Xue JG. Recent progress in organic photovoltaics: device architecture and optical design. *Energ Environ Sci.* 2014;7:2123-2144.
12. Li X, Choy WC, Huo L, et al. Dual plasmonic nanostructures for high performance inverted organic solar cells. *Adv Mater.* 2012;24(22):3046-3052.
13. Atwater HA, Polman A. Plasmonics for improved photovoltaic devices. *Nat Mater.* 2010;9(3):205-213.
14. Gan Q, Bartoli FJ, Kafafi ZH. Plasmonic-enhanced organic photovoltaics: breaking the 10% efficiency barrier. *Adv Mater.* 2013;25(17):2385-2396.
15. Devkota T, Brown BS, Beane G, Yu K, Hartland GV. Making waves: radiation damping in metallic nanostructures. *J Chem Phys.* 2019;151:080901.
16. Zia R, Selker MD, Brongersma ML. Leaky and bound modes of surface plasmon waveguides. *Phys Rev B.* 2005;71:165431.
17. Petoukhoff CE, Shen ZQ, Jain M, Chang AM, O'Carroll DM. Plasmonic electrodes for bulk-heterojunction organic photovoltaics: a review. *J Photon Energy.* 2015;5:057002.

18. Cushing SK, Wu N. Progress and perspectives of plasmon-enhanced solar energy conversion. *J Phys Chem Lett.* 2016;7(4):666-675.
19. Sun Q, Chen JD, Zheng JW, et al. Surface plasmon-assisted transparent conductive electrode for flexible perovskite solar cells. *Adv Opt Mater.* 2019;7:1900847.
20. Ham J, Lee JL. ITO breakers: highly transparent conducting polymer/metal/dielectric (P/M/D) films for organic solar cells. *Adv Energy Mater.* 2014;4:1400539.
21. Bley K, Semmler J, Rey M, et al. Hierarchical design of metal micro/nanohole array films optimizes transparency and haze factor. *Adv Funct Mater.* 2018;28(28):1706965.
22. Tagliabue G, DuChene JS, Abdellah M, et al. Ultrafast hot-hole injection modifies hot-electron dynamics in Au/p-GaN heterostructures. *Nat Mater.* 2020;19(7):1312-1318.
23. Li W, Valentine JG. Harvesting the loss: surface plasmon-based hot electron photodetection. *Nanophotonics.* 2017;6(1):177-191.
24. Besteiro LV, Kong XT, Wang ZM, Hartland G, Govorov AO. Understanding hot-electron generation and plasmon relaxation in metal nanocrystals: quantum and classical mechanisms. *ACS Photonics.* 2017;4(11):2759-2781.
25. Zhang Y, Yam C, Schatz GC. Fundamental limitations to plasmonic hot-carrier solar cells. *J Phys Chem Lett.* 2016;7(10):1852-1858.
26. Ng C, Cadusch JJ, Dligatch S, et al. Hot carrier extraction with plasmonic broadband absorbers. *ACS Nano.* 2016;10(4):4704-4711.
27. Wu K, Chen J, McBride JR, Lian T. Efficient hot-electron transfer by a plasmon-induced interfacial charge-transfer transition. *Science.* 2015;349(6248):632-635.
28. Wang F, Melosh NA. Plasmonic energy collection through hot carrier extraction. *Nano Lett.* 2011;11(12):5426-5430.
29. Stelling C, Singh CR, Karg M, et al. Plasmonic nanomeshes: their ambivalent role as transparent electrodes in organic solar cells. *Sci Rep.* 2017;7:42530.
30. Schubert S, Meiss J, Muller-Meskamp L, Leo K. Improvement of transparent metal top electrodes for organic solar cells by introducing a high surface energy seed layer. *Adv Energy Mater.* 2013;3(4):438-443.
31. Schubert S, Muller-Meskamp L, Leo K. Unusually high optical transmission in Ca:Ag blend films: high-performance top electrodes for efficient organic solar cells. *Adv Funct Mater.* 2014;24(12):6668-6676.
32. Salomon L, Grillot F, Zayats AV, de Fornel F. Near-field distribution of optical transmission of periodic subwavelength holes in a metal film. *Phys Rev Lett.* 2001;86(6):1110-1113.
33. Gao H, McMahon JM, Lee MH, et al. Rayleigh anomaly-surface plasmon polariton resonances in palladium and gold subwavelength hole arrays. *Opt Express.* 2009;17(4):2334-2340.
34. Li Z, Ezhilarasu G, Chatzakis I, et al. Indirect band gap emission by hot electron injection in metal/MoS<sub>2</sub> and metal/WSe<sub>2</sub> heterojunctions. *Nano Lett.* 2015;15(6):3977-3982.
35. Wang M, Ye M, Iocozzia J, Lin C, Lin Z. Plasmon-mediated solar energy conversion via photocatalysis in noble metal/semiconductor composites. *Adv Sci.* 2016;3:1600024.
36. Robatjazi H, Bahauddin SM, Doiron C, Thomann I. Direct plasmon-driven photoelectrocatalysis. *Nano Lett.* 2015;15(9):6155-6161.
37. Lin SS, Lu YH, Xu J, Feng SR, Li JF. High performance graphene/semiconductor van der waals heterostructure optoelectronic devices. *Nano Energy.* 2017;40:122-148.
38. Brongersma ML, Halas NJ, Nordlander P. Plasmon-induced hot carrier science and technology. *Nat Nanotechnol.* 2015;10(1):25-34.
39. Imura K, Okamoto H. Properties of photoluminescence from single gold nanorods induced by near-field two-photon excitation. *J Phys Chem C.* 2009;113(27):11756-11759.
40. Olesiak-Banska J, Waszkielewicz M, Obstarczyk P, Samoc M. Two-photon absorption and photoluminescence of colloidal gold nanoparticles and nanoclusters. *Chem Soc Rev.* 2019;48(15):4087-4117.
41. Bauer M, Marienfeld A, Aeschlimann M. Hot electron lifetimes in metals probed by time-resolved two-photon photoemission. *Prog Surf Sci.* 2015;90(3):319-376.
42. Jiang K, Wei QY, Lai JYL, et al. Alkyl chain tuning of small molecule acceptors for efficient organic solar cells. *Joule.* 2019;3(12):3020-3033.
43. Qin Y, Xu Y, Peng Z, Hou J, Ade H. Low temperature aggregation transitions in N3 and Y6 acceptors enable double-annealing method that yields hierarchical morphology and superior efficiency in nonfullerene organic solar cells. *Adv Funct Mater.* 2020;30:2005011.
44. Furukawa T, Nakanotani H, Inoue M, Adachi C. Dual enhancement of electroluminescence efficiency and operational stability by rapid upconversion of triplet excitons in OLEDs. *Sci Rep.* 2015;5:8429.
45. Cui M, Qin C, Jiang Y, et al. Direct observation of competition between amplified spontaneous emission and auger recombination in quasi-two-dimensional perovskites. *J Phys Chem Lett.* 2020;11(14):5734-5740.

## SUPPORTING INFORMATION

Additional supporting information may be found in the online version of the article at the publisher's website.

**How to cite this article:** Chen J-D, Li L, Qin C-C, et al. Hot-electron emission-driven energy recycling in transparent plasmonic electrode for organic solar cells. *InfoMat.* 2022;1-10. doi:10.1002/inf2.12285